Quantum oscillations and Dirac dispersion in the BaZnBi2 semimetal guaranteed by local Zn vacancy order

K. Zhao, E. Golias, Q. H. Zhang, M. Krivenkov, Anton Jesche, L. Gu, O. Rader, I. I. Mazin, Philipp Gegenwart

Angaben zur Veröffentlichung / Publication details:

Zhao, K., E. Golias, Q. H. Zhang, M. Krivenkov, Anton Jesche, L. Gu, O. Rader, I. I. Mazin, and Philipp Gegenwart. 2018. "Quantum oscillations and Dirac dispersion in the BaZnBi2 semimetal guaranteed by local Zn vacancy order." *Physical Review B* 97 (11): 115166. https://doi.org/10.1103/physrevb.97.115166.

Quantum oscillations and Dirac dispersion in the $BaZnBi_2$ semimetal guaranteed by local Zn vacancy order

K. Zhao,[1] E. Golias,[2,3] Q. H. Zhang,[4] M. Krivenkov,[2] A. Jesche,[1] L. Gu,[4] O. Rader,[2] I. I. Mazin,[5] and P. Gegenwart[1]

[1]*Experimentalphysik VI, Center for Electronic Correlations and Magnetism, University of Augsburg, 86159 Augsburg, Germany*

[2]*Helmholtz-Zentrum Berlin für Materialien und Energie, Elektronenspeicherring BESSY II, Albert-Einstein-Straße 15, 12489 Berlin, Germany*

[3]*Institut für Experimentalphysik, Freie Universität Berlin, Arnimallee 14, 14195 Berlin, Germany*

[4]*Beijing National Laboratory for Condensed Matter Physics, Institute of Physics, Chinese Academy of Sciences, Beijing 100190, China*

[5]*Naval Research Laboratory, Code 6390, 4555 Overlook Avenue SW, Washington, DC 20375, USA*

(Received 18 January 2018; published 30 March 2018)

We have synthesized single crystals of Dirac semimetal candidates $AZnBi_2$ with A = Ba and Sr. In contrast to A = Sr, the Ba material displays a local Zn vacancy ordering, which makes the observation of quantum oscillations in out-of-plane magnetic fields possible. As a Dirac semimetal candidate, $BaZnBi_2$ exhibits a small cyclotron electron mass, high quantum mobility, and nontrivial Berry phases. Three Dirac dispersions are observed by angle-resolved photoemission spectroscopy and identified by first-principles band-structure calculations. Compared to $AMn(Bi/Sb)_2$ systems which host Mn magnetic moments, $BaZnBi_2$ acts as a nonmagnetic analog to investigate the intrinsic properties of Dirac fermions in this structure family.

DOI: 10.1103/PhysRevB.97.115166

Topological materials, such as Dirac and Weyl semimetals, have received increasing attention in recent years due to their special physical properties and potential applications [1–12]. In such systems, the electron transport is often dominated by linearly dispersing Dirac or Weyl fermions, leading to quantum oscillations with nontrivial Berry phases, quantum Hall effect, and negative magnetoresistance [1–12].

Recently, the layered manganese pnictides $AMn(Bi/Sb)_2$ (A = Ca, Sr, Ba, Eu, and Yb) were reported to host Dirac or Weyl fermions, related to their two-dimensional (2D) Bi/Sb layers [13–30]. Common structural features for all of these compounds are magnetic MnBi/Sb layers intercalated by 2D Bi/Sb layers. The latter have been shown to host quasi-2D Dirac fermions, similar as in graphene and topological insulators [11–13]. Moreover, the interplay between magnetism and the Dirac dispersion induces interesting quantum states: $EuMnBi_2$ shows a bulk half-integer quantum Hall effect due to magnetically confined 2D Dirac fermions [21]. A canted antiferromagnetic order with a ferromagnetic component coexists with the Dirac fermion behavior in $Sr_{1-y}Mn_{1-z}Sb_2$ [25]. Moreover, $YbMnBi_2$ probably features a time-reversal symmetry breaking Weyl fermion state, because the spin degeneracy is lifted by a similar ferromagnetic component [26].

Up to now, all studied compounds of this structure family contain both magnetic MnBi/Sb layers and 2D Bi/Sb layers. To achieve a full understanding of the interplay between the magnetism and Dirac dispersion [31,32], it is instructive to investigate materials without magnetic Mn. This addresses the question, whether a two-dimensional Bi/Sb layer without a magnetic layer still holds Dirac fermions, and if so, to compare its properties with those of the magnetic materials.

Based on powder samples, $BaZnBi_2$ and $SrZnBi_2$ were reported to crystallize in the same tetragonal structure as $SrMnBi_2$ [33]. In this article, we report a single crystal study of both materials. While $SrZnBi_2$ shows the expected tetragonal structure with the space group $I4/mmm$, $BaZnBi_2$ forms local Zn vacancies, which order along a face diagonal direction. This ordering has important consequences regarding the physical properties of the two sister compounds. Due to the random Zn vacancies, quantum oscillations are not detectable in $SrZnBi_2$. By contrast, pronounced de Haas–van Alphen (dHvA) and Shubnikov–de Haas (SdH) oscillations were observed in $BaZnBi_2$ for the out-of-plane field orientation. Analyzing the dHvA and SdH oscillations, we find key signatures of Dirac fermions, including a light effective mass ($\sim 0.1 m_e$, where m_e is the free-electron mass), high quantum mobility (684 $cm^2\,V^{-1}\,s^{-1}$), and a nonzero Berry phase accumulated along the cyclotron orbit. Furthermore, we directly probe the Dirac dispersion by angle-resolved photoemission spectroscopy (ARPES) and identify the responsible bands by first-principles density functional theory calculations.

Figure 1(a) shows the x-ray diffraction pattern of single-crystalline $BaZnBi_2$, with only $(00L)$ reflections observed, in line with the expected preferred orientation of platelike crystals. $SrZnBi_2$ has a tetragonal structure similar to that of $SrMnBi_2$, as only $(0,0,2L)$ peaks are visible in Fig. 1(b), consistent with the diffraction pattern of the space group $I4/mmm$. The lattice parameters of $BaZnBi_2$ agree with those reported in Ref. [33], $a = b = 4.847$ Å, and $c = 21.98$ Å. However, Fig. 1(a) clearly indicates the presence of $(0,0,2L+1)$ peaks as well, signaling a new structural modulation in $BaZnBi_2$, which had not been detected in powder samples.

We have measured selected area electron diffraction (SAED) along the [110] direction in Fig. 1(c), on a circle area with a radius of roughly 200 nm. Consistent with x-ray diffraction patterns, (001), (002), and (003), etc., the corresponding SAED reflections are also visible. Weak but clear diffraction peaks appear at $(H,-H,0)$ (H = half integer), indicating the existence of a modulated structure doubling the

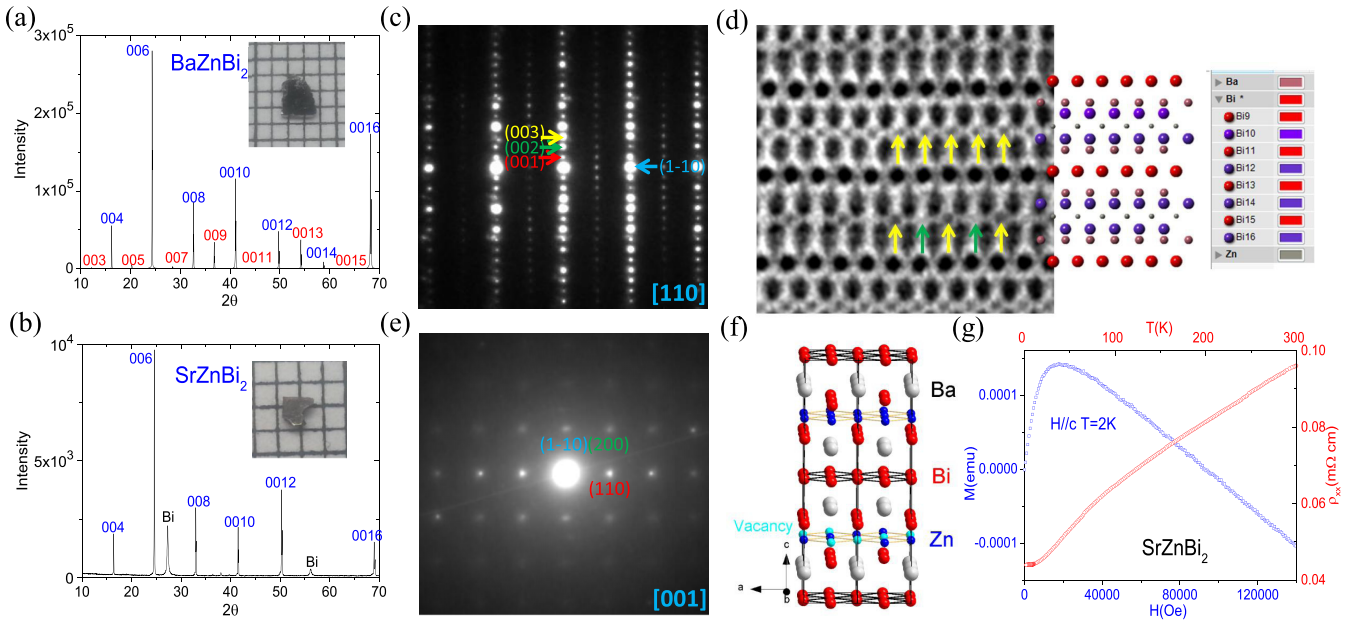

FIG. 1. (a), (b) Single-crystal XRD pattern of $BaZnBi_2$ and $SrZnBi_2$, with an optical image of a typical single crystal as an inset. (c) Selected area electron diffraction (SAED) pattern along the [110] direction. (d) Corresponding atomic resolution scanning transmission electron microscope (STEM) image, with the yellow arrow indicating the Zn site and the green arrow indicating the Zn vacancy site. (e) SAED pattern along the [001] direction. (f) Crystal structure of $BaZnBi_2$ in the local Zn vacancy order region, with vacancy positions indicated by light blue circles. (g) Left: Isothermal out-of-plane ($H \parallel c$) magnetization for $SrZnBi_2$ at 2 K. Right: In-plane resistivity (ρ_{xx}) of $SrZnBi_2$ between 2 and 300 K (see text).

unit cell along a face diagonal direction, compared to the space group $I4/mmm$.

Next, we employed atomic resolution scanning transmission electron microscopy (STEM) to directly probe the modulated structure of $BaZnBi_2$ in real space, for a thinned crystal with a thickness of about 50 nm. As shown in Fig. 1(d), the atomic arrangements of Bi and Ba columns are in good agreement with the standard tetragonal structure, while an ordering of Zn vacancies appears in every second Zn layer. Contrary to the occupied sizes, indicated by yellow arrows, the sites marked by green arrows are unoccupied. The [110] direction is the face diagonal direction of the tetragonal structure, and the Zn vacancies also order along this direction, as illustrated in Fig. 1(f).

After the observation of Zn vacancy order in certain local regions, to investigate whether this structural feature forms a long-range order, we have measured SAED along the [001] direction on several different circle areas with a radius of roughly 300 nm. In Fig. 1(e), the diffraction pattern is consistent with that of the space group $I4/mmm$ in the ab plane, with no diffraction peaks at $(H,-H,0)$ (H = half integer), indicating the absence of structural modulation in the ab plane of $BaZnBi_2$. In Fig. 1(b), we observe a weak diffraction peak at $(1/2,-1/2,0)$ in the [110] direction; however, this diffraction peak does not appear in the [001] direction. Thus, combining the SAED pattern along both [110] and [001] directions, we conclude that the Zn vacancy ordering has a local character and is not uniform, not forming a long-range structure in $BaZnBi_2$. This local Zn vacancy ordering causes large differences in the physical property between $BaZnBi_2$ and $SrZnBi_2$.

There is no indication of quantum oscillations in the isothermal magnetization up to 14 T for $SrZnBi_2$ (at 2 K in out-of-plane orientation) in Fig. 1(g). In fact, the in-plane residual resistance ratio (RRR) $= R(300\ \mathrm{K})/R(2\ \mathrm{K}) = 2.3$ is much smaller compared to 8 for $SrMnBi_2$ and $CaMnBi_2$ [13–16], indicating strong scattering, presumably from a large number of disorder Zn vacancies.

Figure 2(a) shows the isothermal magnetization measured up to 14 T for $BaZnBi_2$ in $H \parallel c$. The magnetization exhibits strong dHvA oscillations, which start around 5 T and persist up to 25 K, similar as found for $CaMnBi_2$ and $SrMnSb_2$ [16,25]. In Fig. 2(b), we present the oscillatory component of magnetization for $BaZnBi_2$ at 2 K, obtained after subtracting the background between 7 and 14 T. From the fast Fourier transformation (FFT) analysis in Fig. 2(c), three frequencies 168, 196, and 238 T are derived, comparable to the dHvA frequencies 101 and 181 T measured in $CaMnBi_2$ [16] and the SdH frequency of 152 T in $SrMnBi_2$ [13] for the same field orientation. Evidence for Dirac fermions in $BaZnBi_2$ has been obtained from the further analysis of the dHvA oscillations. As shown in Fig. 2(d), the effective cyclotron mass m^* can be extracted from the fit of the temperature dependence of the normalized FFT peak amplitude according to the thermal damping factor in the Lifshitz-Kosevich (LK) equation, i.e., $\Delta M/M_0 \propto AT\mu/B/[\sinh(AT\mu/B)]$, where $A = 2\pi^2 k_B m_e/\hbar e$ is the thermal factor, and μ is the ratio of effective mass to the free-electron mass. We calculated the FFT within the field range 7–14 T, with an average $B = 9.33$ T and obtained effective masses $m^* = 0.127m_e$ for the 196 T peak, $0.170m_e$ for 168 T, and $0.124m_e$ for the 238 T orbits [see Fig. 2(d)]. The effective mass in $BaZnBi_2$ is thus smaller

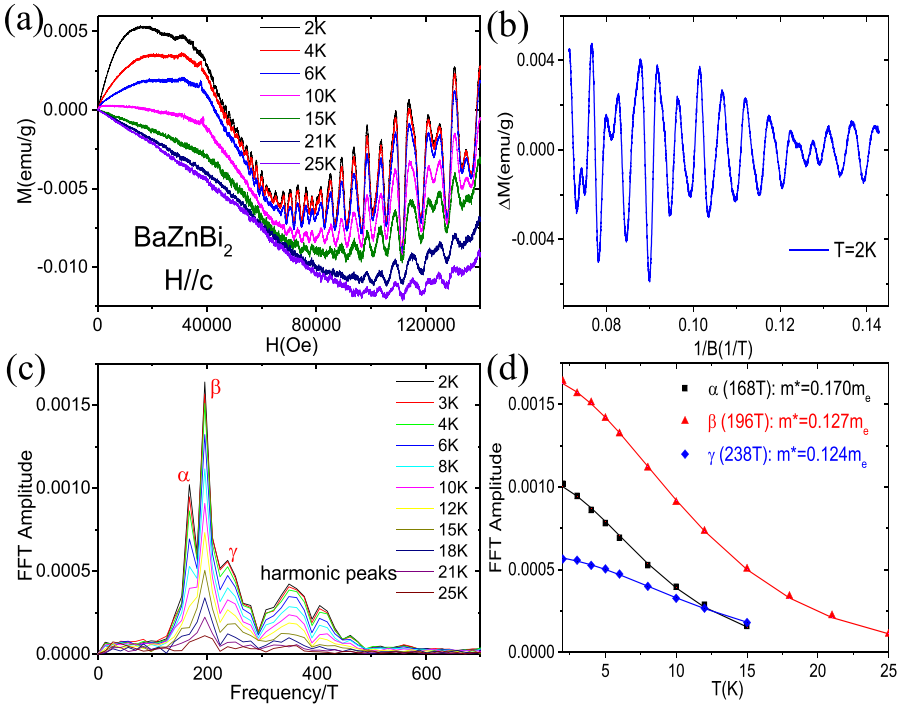

FIG. 2. (a) Isothermal out-of-plane ($H \parallel c$) magnetization for $BaZnBi_2$ at various temperatures. (b) Oscillatory component of magnetization for $BaZnBi_2$ at 2 K between 7 and 14 T. (c) FFT spectra of $\Delta M(B)$ at different temperatures (the FFT was done in the field range between 7 and 14 T). (d) The temperature dependence of the normalized FFT amplitude for α, β, and γ oscillations, with fitting to the Lifshitz-Kosevich (LK) formula (see text).

than that in $SrMnBi_2$ ($0.29m_e$) [13] and in $CaMnBi_2$ ($0.35m_e$) [15,16], and comparable to $0.105m_e$ in $BaMnBi_2$ [23] and $0.14m_e$ in $SrMnSb_2$ [25].

Due to the formation of a local Zn vacancy order in $BaZnBi_2$, the scattering is greatly reduced, and the in-plane resistivity $\rho_{xx}(T)$ [Fig. 3(a)] is metallic with a RRR about 7, comparable to that of (Ca/Sr/Ba)$MnBi_2$ [13–16,23]. The out-of-plane resistivity is larger than the in-plane resistivity, with $\rho_c(T)/\rho_{xx}(T)$ increasing from less than 10 at 300 K to more than 50 at 2 K.

As (Ca/Sr/Ba)Mn(Bi/Sb)$_2$ [13–28], $BaZnBi_2$ also exhibits quantum transport behaviors. As shown in Fig. 3(b), a systematic evolution of magnetoresistance is observed in a magnetic field rotating from the c axis to the ab plane direction [see the insets of Fig. 3(b) regarding the experimental setup with $B \parallel I$ for $\theta = 90°$]. The SdH oscillatory component is shown in Fig. 3(c) between 7 and 14 T with $H \parallel c$. The oscillation frequency is 168 T, exactly the same as one of the frequencies of the dHvA oscillations. Furthermore, the oscillation frequency $F(\theta)$ extracted from ρ_{xx} can be fitted to $F(\theta) = F(0°)/\cos\theta$ [inset of Fig. 3(d)], suggesting that the Fermi surface responsible for the SdH oscillations is either a two-dimensional (2D) cylindrical shape or an elongated elliptical shape. Note there is another oscillation with the frequency 30 T that does not change with the magnetic field rotation. Similar to other Bi/Sb layer semimetals [13–28], the angular magnetoresistance (AMR) of $BaZnBi_2$ at 2 K in 7 T, shown in Supplemental Fig. S1(a) follows a [$\cos(\theta)$] dependence very well, with a typical twofold anisotropy expected for a material with a quasi-2D electronic structure.

Besides the small effective electron mass, Dirac fermions also have a high quantum mobility. This holds, for instance, in topological insulators and in Cd_3As_2 [7,12] and is also verified in $BaZnBi_2$. The quantum mobility is related to the quantum relaxation time τ_q by $\mu_q = e\tau_q/m^*$, which could be found from the field damping of the quantum oscillation amplitude, i.e., $\Delta\rho/\rho_0 \propto \exp(-AT_D\mu/B)\, AT\mu/B/[\sinh(AT\mu/B)]$. T_D is the Dingle temperature and is linked to τ_q as $T_D = h/(2pkB\tau_q)$. With m^* already known, τ_q at 2 K can be extracted through the linear fit of $\ln([B\sinh(AT\mu/B)/AT\mu]\,\Delta\rho/\rho_0)$ against $1/B$. As shown in Fig. 3(e), we have obtained $T_D = 15.7$ K, $\tau_q = 6.4 \times 10^{-14}$ s, from which the quantum mobility μ_q ($=e\tau_q/m^*$) is estimated to be 684 $cm^2\,V^{-1}\,s^{-1}$, comparable to that of $SrMnBi_2$ (250 $cm^2\,V^{-1}\,s^{-1}$) and $SrMnSb_2$ (570 $cm^2\,V^{-1}\,s^{-1}$) [13,25]. Compared with the strong dHvA oscillations, the SdH oscillations of $BaZnBi_2$ are relatively weak, probably associated with the strong background magnetoresistance, similar in the nodal line semimetal ZrSiS/Se/Te case [34–36]. As discussed before, the scattering has been greatly reduced due to the local vacancy order in $BaZnBi_2$; however, there is still some scattering, especially at the boundary of Zn vacancy order region. The 196 and 238 T oscillations in magnetization probably arise from bands which are more sensitive to such scattering in the transport experiment. Another possibility is that a higher magnetic field is needed to observe them in SdH oscillations. As discussed below, the single dominant SdH frequency actually allows us to extract the respective Berry phase.

To verify the topological nature of the nearly massless electrons in $BaZnBi_2$, we extracted the Berry phase accumulated along the cyclotron orbit from the analysis of SdH oscillations. We present the Landau level (LL) fan diagram constructed from the SdH oscillations of ρ_{xx} for $BaZnBi_2$ in Fig. 3(f), where the integer LL indices are assigned to the maxima of ρ_{xx}. The definition of a LL index is based upon a customary practice whereby integer LL indices are assigned to conductivity minima [37]. The in-plane conductivity σ_{xx} can be calculated from the longitudinal resistivity ρ_{xx} and the transverse (Hall) resistivity ρ_{xy} as $\sigma_{xx} = \rho_{xx}/(\rho_{xx}^2 + \rho_{xy}^2)$.

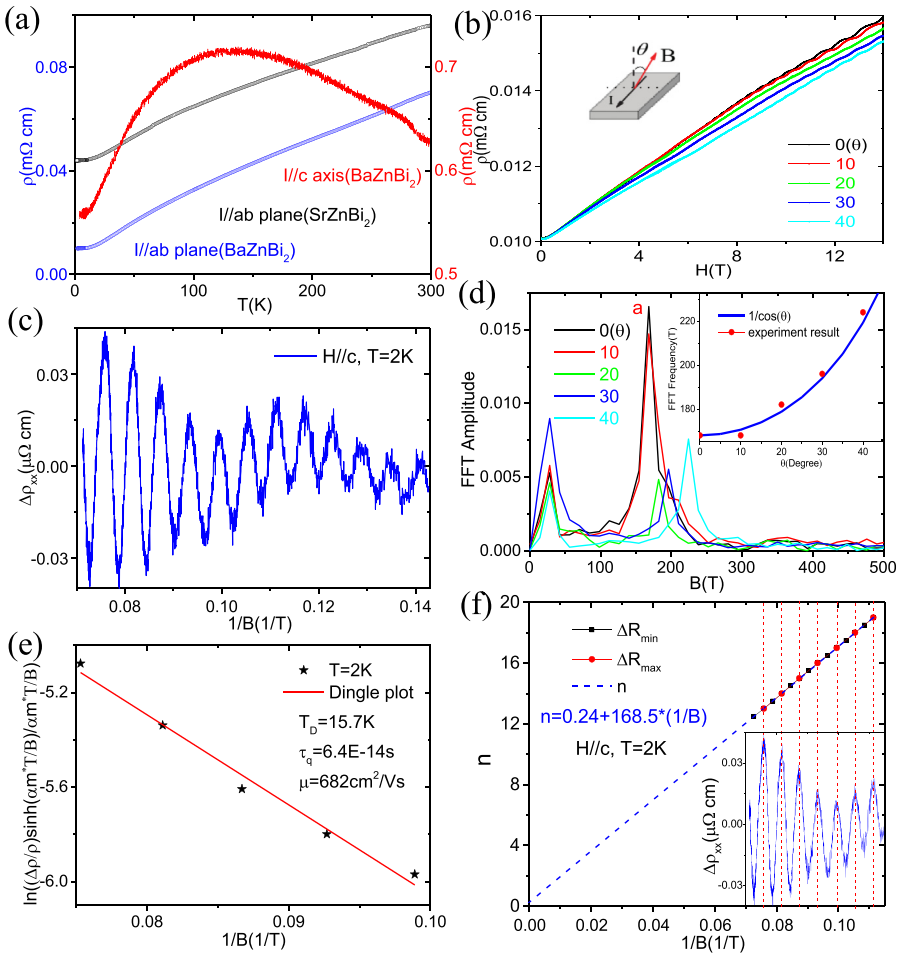

FIG. 3. (a) In-plane resistivity (ρ_{xx}) and out-of-plane resistivity (ρ_c) of $BaZnBi_2$ as a function of temperature, with ρ_{xx} of $SrZnBi_2$ as a comparison. (b) Magnetoresistance measured under different field orientations, with the diagram of the measurement setup as the inset. θ is defined as the angle between the magnetic field and the out-of-plane direction. (c) The oscillation component of in-plane resistivity ρ_{xx} vs $1/B$ measured for $H \parallel c$ at 2 K. (d) The FFT spectra of $\Delta\rho_{xx}(B)$ at different field orientations. Inset: The angular dependence of the SdH oscillation frequency. The dashed curve is a fit to $F(\theta) = F(0^\circ)/\cos\theta$. (e) Dingle plot for the in-plane quantum oscillations ρ_{xx} at 2 K. (f) Landau level (LL) fan diagram. The blue dashed line represents the linear fit, with integer LL indices assigned to the maximum of resistivity (see text).

According to Fig. S1(b) [38], ρ_{xy} is less than $0.1\rho_{xx}$ for $B < 14$ T, and $\sigma_{xx} \approx 1/\rho_{xx}$, thus the conductivity minima correspond to the ρ_{xx} maxima. As shown in Fig. 3(f), the intercept on the LL index axis obtained from the extrapolation of the linear fit in the fan diagram is 0.24, corresponding to a $0.5(1)\pi$ Berry phase, which is smaller than the expected value of π for a 2D Dirac system. As in $BaMnBi_2$ [23], this is likely due to the large contribution of parabolic bands at the Fermi level, which is further verified by the first-principles calculations below. Another possibility is a deviation of the Dirac band from pure linearity close to the Dirac point, arising from a small spin-orbit gap as discussed below. The oscillation frequency derived from the fit is 168.5 T, nearly the same as the frequency obtained from the SdH oscillations, emphasizing the reliability of our linear fit in the fan diagram.

The band structure of $BaZnBi_2$ has been calculated from first-principles using the standard linearized augmented plane-wave code WIEN2K [39], including spin-orbit coupling (SOC). As indicated in Fig. 1, the local Zn vacancy ordering does not form a long-range structure in $BaZnBi_2$. Moreover, the Zn content does not show an obvious decrease, compared with Ba in the energy-dispersive x-ray spectrometer (EDX) measurement. Thus, the composition could be written as $BaZn_{1-x}Bi_2$ ($x < 0.1$), for simplicity still using $BaZnBi_2$. With most parts of the system being uniform without Zn vacancies and generating the quantum oscillations, we adopt the $I4/mmm$ tetragonal structure without Zn vacancies to calculate the band structure. Similar to $SrMnBi_2$ and $CaMnBi_2$ [19,20], the low-energy states are formed mainly by the Bi orbitals of the 2D Bi layer. The SOC in Bi opens a gap between the upper and lower Dirac branches. Formally, $BaZnBi_2$ is not a Dirac semimetal, such as Cd_3As_2 [2,3,7], but the SOC gap is small enough for its transport properties to be similar to a real case, so we use the term *Dirac semimetal candidate* throughout the paper. According to the calculations (Fig. 4), there are two Dirac points near X, and one along the ΓM direction, quite similar to the isostructural $SrMnBi_2$ [20]. The 2D isoenergetic contours for $k_z = 0$ are presented in Supplemental Fig. S2, and bear further evidence to the presence of Dirac bands. Indeed, the contour corresponding to $E - E_F = 30$ meV shows Dirac bands in the ΓX and ΓM direction, and that at the 35 meV plot contains three Dirac bands in the ΓX, XM, and ΓM direction, respectively [38].

In Figs. 5(b)–5(e), we present the ARPES results, including the Fermi surface and constant energy contours of $BaZnBi_2$ at binding energies of 90, 200, and 300 meV, respectively. In Fig. 5(b), arrows indicate a faint electronic state that rims the Fermi surface. In the vicinity of this faint state there is an intense electronic state in smaller k values and four electron pockets at the X points of the surface Brillouin zone (SBZ). We can also see two holelike states centered at the Γ point of the SBZ. On the other hand, the two outer electronic states with the

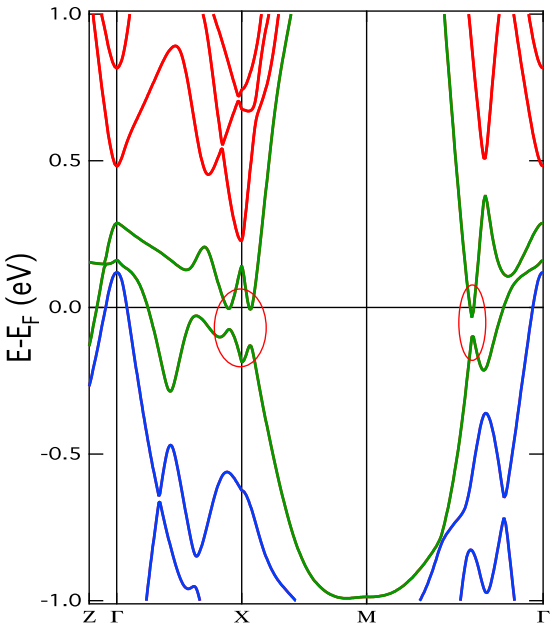

FIG. 4. Band structure of $BaZnBi_2$ calculated including SOC with Dirac bands marked by red circles (see text).

distorted rhombus shape have an opposite dispersion and merge at a binding energy of 200 meV. These states can be also seen along different high-symmetry directions forming Dirac-like dispersions that cross the Fermi level. More specifically, in Figs. 5(g)–5(j), we present the band dispersions along the high-symmetry XM, ΓX, and ΓM directions, with black arrows indicating the crossing of the two distorted rhombus bands seen in Figs. 5(b) and 5(c). The apparent Dirac-like feature around the X point in Fig. 5(g) comes from the anisotropic Dirac states in $BaZnBi_2$, as already observed in $SrMnBi_2$ and $CaMnBi_2$ [13,19,20]. Correspondingly, we observe the band crossing point moving towards the Fermi level in the line dispersion parallel to the XM direction close to the center of the electron pocket in Fig. 5(h), which does not show the expected gap opening from an isotropic Dirac band, such as in graphene, topological insulators, and Cd_3As_2 [3,11,12]. Concerning the band dispersion along the ΓM direction in Fig. 5(j), the band crossing is barely seen due to matrix element effects—the parabolic bands that cross the Fermi level along ΓM can be better seen if one moves off center (see Fig. S4) [38]. As shown in Supplemental Fig. S2(d) [38], for the holelike bands at the Γ point, the constant energy contour plot taken with $k_z = 0.4\pi/c$ matches better the ARPES results presented in Figs. 5(b)–5(d), an indication that the excitation energy used in our ARPES measurements corresponds to a k_z that intersects off center the three-dimensional Brillouin zone. In principle, our ARPES data are in good agreement with the dHvA oscillations and theoretical calculation results, as we observe three Dirac-like states that contribute to quantum oscillations, namely, one along the XM direction in Fig. 5(g), another one along the ΓX direction in Fig. 5(i), and the third one along the ΓM direction in Fig. 5(j), respectively.

In conclusion, contrary to the general belief that vacancies usually prohibit the detection of intrinsic properties of a system, just as for the $SrZnBi_2$ case, we identify that the local

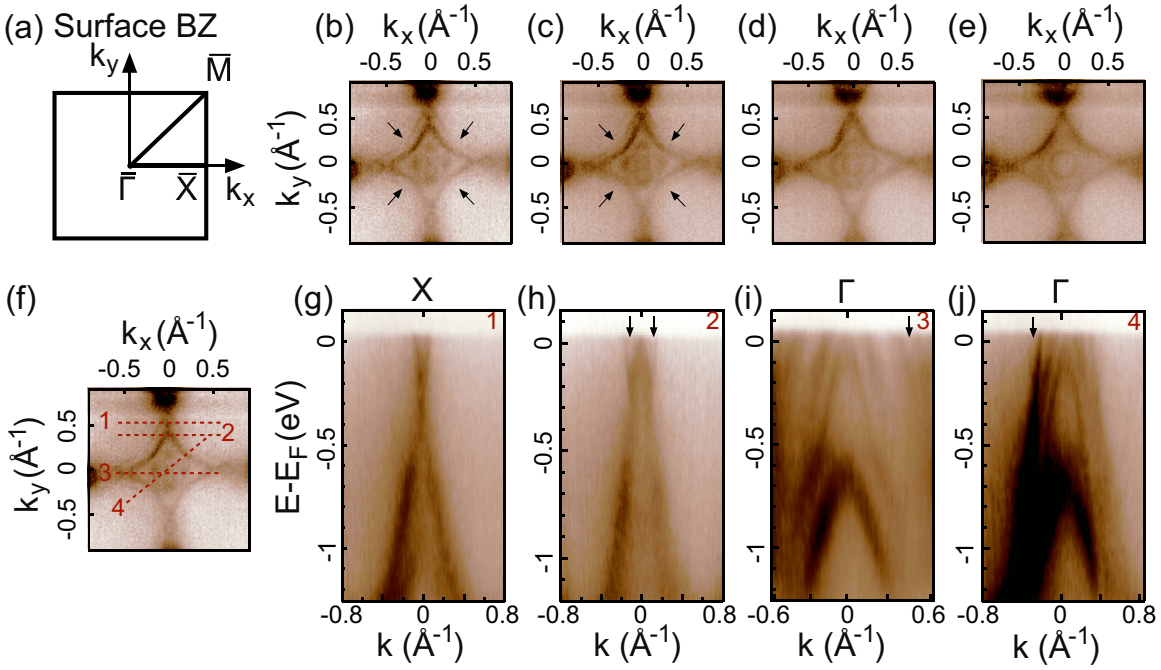

FIG. 5. ARPES results: (a) Sketch of the $BaZnBi_2$ (001) surface Brillouin zone corresponding to the high-symmetry directions presented in the constant energy contours of (b)–(e). (b)–(e) Constant energy contour plots at binding energies of 0, 90, 200, and 300 meV, respectively, obtained using horizontally polarized light with $h\nu = 75$ eV, with black arrows indicating the faint distorted rhombus bands in (b) and (c). (f) Red dashed numbered lines on the Fermi surface of $BaZnBi_2$ highlight the lines of the corresponding band dispersion shown in (g)–(j), with black arrows indicating the crossing of the two distorted rhombus bands seen in (b) and (c).

Zn vacancy order guarantees the dHvA and SdH oscillations in a nontrivial system $BaZnBi_2$, exhibiting a light effective mass ($\sim 0.1 m_e$), high quantum mobility (684 $cm^2\,V^{-1}\,s^{-1}$), and a nonzero Berry phase accumulated along the cyclotron orbit. Further consistent with band-structure calculations, the Dirac dispersion is directly observed by ARPES. The Dirac semimetal candidate $BaZnBi_2$ seems to be a promising platform to investigate the intrinsic properties of Dirac fermions. Because of the similar quantum oscillations and Dirac dispersion in $BaZnBi_2$ compared to $AMn(Bi/Sb)_2$ (A = Ca, Sr, Ba, Eu, and Yb), our results clearly indicate that the Dirac fermions in the two-dimensional Bi/Sb layers are not influenced by the antiferromagnetism in the MnBi/Sb layer, except for the canted case in $YbMnBi_2$ [26].

Note added. Recently, we became aware of two papers about $BaZnBi_2$ [40,41], which show quantum oscillation results. However, with the presence of $(0,0,2L+1)$ peaks in the single-crystal x-ray diffraction pattern, both papers do not mention the existence of local Zn vacancy order.

The authors would like to thank Peizhe Tang, Philip Moll, Yurii Skourski, Jin Hu, Hongbin Zhang, Qiang Zou, and Jinguang Cheng for helpful discussions and experimental collaborations. The work was supported by the German Science Foundation through the priority program SPP 1666 and the Emmy Noether program JE 748/1. Work at IOP was supported by the Strategic Priority Research Program of the Chinese Academy of Sciences (Grant No. XDB07030200), and the National Natural Science Foundation of China (Grant No. 51522212). I.I.M. acknowledges funding from the Office of Naval Research (ONR) through the Naval Research Laboratory's Basic Research Program.

[1] Z. Wang, Y. Sun, X.-Q. Chen, C. Franchini, G. Xu, H. Weng, X. Dai, and Z. Fang, Phys. Rev. B **85**, 195320 (2012).
[2] Z. Wang, H. Weng, Q. Wu, X. Dai, and Z. Fang, Phys. Rev. B **88**, 125427 (2013).
[3] Z. Liu, J. Jiang, B. Zhou, Z. Wang, Y. Zhang, H. Weng, D. Prabhakaran, S. K. Mo, H. Peng, P. Dudin *et al.*, Nat. Mater. **13**, 677 (2014).
[4] Z. Liu, B. Zhou, Y. Zhang, Z. Wang, H. Weng, D. Prabhakaran, S.-K. Mo, Z. Shen, Z. Fang, X. Dai *et al.*, Science **343**, 864 (2014).
[5] M. N. Ali, Q. Gibson, S. Jeon, B. B. Zhou, A. Yazdani, and R. Cava, Inorg. Chem. **53**, 4062 (2014).
[6] M. Neupane, S.-Y. Xu, R. Sankar, N. Alidoust, G. Bian, C. Liu, I. Belopolski, T.-R. Chang, H.-T. Jeng, H. Lin *et al.*, Nat. Commun. **5**, 3786 (2014).
[7] T. Liang, Q. Gibson, M. N. Ali, M. Liu, R. Cava, and N. Ong, Nat. Mater. **14**, 280 (2015).
[8] H. Weng, C. Fang, Z. Fang, B. A. Bernevig, and X. Dai, Phys. Rev. X **5**, 011029 (2015).
[9] B. Lv, H. Weng, B. Fu, X. Wang, H. Miao, J. Ma, P. Richard, X. Huang, L. Zhao, G. Chen *et al.*, Phys. Rev. X **5**, 031013 (2015).
[10] S.-Y. Xu, I. Belopolski, N. Alidoust, M. Neupane, G. Bian, C. Zhang, R. Sankar, G. Chang, Z. Yuan, C.-C. Lee *et al.*, Science **349**, 613 (2015).
[11] Y. Zhang, Y.-W. Tan, H. L. Stormer, and P. Kim, Nature (London) **438**, 201 (2005).
[12] X.-L. Qi and S.-C. Zhang, Rev. Mod. Phys. **83**, 1057 (2011).
[13] J. Park, G. Lee, F. Wolff-Fabris, Y. Koh, M. Eom, Y. Kim, M. Farhan, Y. Jo, C. Kim, J. Shim *et al.*, Phys. Rev. Lett. **107**, 126402 (2011).
[14] K. Wang, D. Graf, H. Lei, S. W. Tozer, and C. Petrovic, Phys. Rev. B **84**, 220401 (2011).
[15] K. Wang, D. Graf, L. Wang, H. Lei, S. W. Tozer, and C. Petrovic, Phys. Rev. B **85**, 041101(R) (2012).
[16] J. He, D. Wang, and G. Chen, Appl. Phys. Lett. **100**, 112405 (2012).
[17] G. Lee, M. A. Farhan, J. S. Kim, and J. H. Shim, Phys. Rev. B **87**, 245104 (2013).
[18] Y. F. Guo, A. J. Princep, X. Zhang, P. Manuel, D. Khalyavin, I. I. Mazin, Y. G. Shi, and A. T. Boothroyd, Phys. Rev. B **90**, 075120 (2014).
[19] L.-L. Jia, Z.-H. Liu, Y.-P. Cai, T. Qian, X.-P. Wang, H. Miao, P. Richard, Y.-G. Zhao, Y. Li, D.-M. Wang *et al.*, Phys. Rev. B **90**, 035133 (2014).
[20] Y. Feng, Z. Wang, C. Chen, Y. Shi, Z. Xie, H. Yi, A. Liang, S. He, J. He, Y. Peng *et al.*, Sci. Rep. **4**, 5385 (2014).
[21] H. Masuda, H. Sakai, M. Tokunaga, Y. Yamasaki, A. Miyake, J. Shiogai, S. Nakamura, S. Awaji, A. Tsukazaki, H. Nakao *et al.*, Sci. Adv. **2**, e1501117 (2016).
[22] J. Liu, J. Hu, H. Cao, Y. Zhu, A. Chuang, D. Graf, D. Adams, S. Radmanesh, L. Spinu, I. Chiorescu *et al.*, Sci. Rep. **6**, 30525 (2016).
[23] L. Li, K. Wang, D. Graf, L. Wang, A. Wang, and C. Petrovic, Phys. Rev. B **93**, 115141 (2016).
[24] A. Wang, I. Zaliznyak, W. Ren, L. Wu, D. Graf, V. O. Garlea, J. B. Warren, E. Bozin, Y. Zhu, and C. Petrovic, Phys. Rev. B **94**, 165161 (2016).
[25] J. Liu, J. Hu, Q. Zhang, D. Graf, H. Cao, S. Radmanesh, D. Adams, Y. Zhu, G. Cheng, X. Liu *et al.*, Nat. Mater. **16**, 905 (2017).
[26] S. Borisenko, D. Evtushinsky, Q. Gibson, A. Yaresko, T. Kim, M. N. Ali, B. Buechner, M. Hoesch, and R. J. Cava, arXiv:1507.04847.
[27] S. Huang, J. Kim, W. Shelton, E. Plummer, and R. Jin, Proc. Natl. Acad. Sci. U.S.A. **114**, 6256 (2017).
[28] J. He, Y. Fu, L. Zhao, H. Liang, D. Chen, Y. Leng, X. Wang, J. Li, S. Zhang, M. Xue *et al.*, Phys. Rev. B **95**, 045128 (2017).
[29] J. Liu, J. Hu, D. Graf, T. Zou, M. Zhu, Y. Shi, S. Che, S. Radmanesh, C. Lau, L. Spinu *et al.*, Nat. Commun. **8**, 646 (2017).
[30] R. Kealhofer, S. Jang, S. M. Griffin, C. John, K. A. Benavides, S. Doyle, T. Helm, P. J. Moll, J. B. Neaton, J. Y. Chan *et al.*, Phys. Rev. B **97**, 045109 (2018).
[31] A. Zhang, C. Liu, C. Yi, G. Zhao, T.-l. Xia, J. Ji, Y. Shi, R. Yu, X. Wang, C. Chen *et al.*, Nat. Commun. **7**, 13833 (2016).
[32] M. C. Rahn, A. J. Princep, A. Piovano, J. Kulda, Y. F. Guo, Y. G. Shi, and A. T. Boothroyd, Phys. Rev. B **95**, 134405 (2017).
[33] E. Brechtel, G. Cordier, and H. Schäfer, J. Less Common Met. **79**, 131 (1981).
[34] J. Hu, Z. Tang, J. Liu, X. Liu, Y. Zhu, D. Graf, K. Myhro, S. Tran, C. N. Lau, J. Wei *et al.*, Phys. Rev. Lett. **117**, 016602 (2016).

[35] J. Hu, Z. Tang, J. Liu, Y. Zhu, J. Wei, and Z. Mao, Phys. Rev. B **96**, 045127 (2017).

[36] J. Hu, Y. L. Zhu, D. Graf, Z. J. Tang, J. Y. Liu, and Z. Q. Mao, Phys. Rev. B **95**, 205134 (2017).

[37] Y. Ando, J. Phys. Soc. Jpn. **82**, 102001 (2013).

[38] See Supplemental Material at http://link.aps.org/supplemental/10.1103/PhysRevB.97.115166 for additional details about single-crystal growth, x-ray diffraction, magnetization, resistivity, TEM, and ARPES measurements.

[39] P. Blaha, K. Schwarz, G. Madsen, D. Kvasnicka, and J. Luitz, *WIEN2k, An Augmented Plane Wave+Local Orbitals Program for Calculating Crystal Properties*, edited by K. Schwarz (Techn. Universität Wien, Austria, 2001).

[40] Y.-Y. Wang, P.-J. Guo, Q.-H. Yu, S. Xu, K. Liu, and T.-L. Xia, New J. Phys. **19**, 123044 (2017).

[41] W. Ren, A. Wang, D. Graf, Y. Liu, Z. Zhang, W.-G. Yin, and C. Petrovic, Phys. Rev. B **97**, 035147 (2018).